Supplemental Material for

Lattice dynamics and structural transition of the hyperhoneycomb iridate β-Li_2IrO_3 investigated by high-pressure Raman scattering

Sungkyun Choi,[1,*] Heung-Sik Kim,[2,3] Hun-Ho Kim,[1] Aleksandra Krajewska,[1] Gideok Kim,[1] Matteo Minola,[1] Tomohiro Takayama,[1] Hidenori Takagi,[1] Kristjan Haule,[2] David Vanderbilt,[2] and Bernhard Keimer[1]

[1] *Max Planck Institute for Solid State Research, Heisenbergstrasse 1, 70569 Stuttgart, Germany*
[2] *Department of Physics and Astronomy, Rutgers University, Piscataway, New Jersey 08854-8019, USA*
[3] *Department of Physics, Kangwon National University, 1 Gangwondaehak-gil, Chuncheon-si, Gangwon-do 24341, Republic of Korea*

(Dated: July 28, 2019)

This Supplemental Material present the full technical details of single crystal growth and characterization in Section S1, Raman beam-heating measurements in Section S2, Raman experiments in Section S3, followed by details for structural relaxations in Section S4 and phonon calculations in Section S5, and *ab-initio* calculations in Section S6. Tables provide DFT/DMFT-optimized crystal structures, fitted peak positions from the beam-heating measurements, calculated Raman-active phonons and fitted Raman frequencies with the green Raman light.

S1. SINGLE CRYSTAL GROWTH AND CHARACTERIZATION

High-quality single crystals were synthesized by a flux-method explained elsewhere.[1] The crystallographic axes of the single crystals were determined by single crystal x-ray diffraction and polarization-resolved Raman measurements by means of the Raman selection rules.[2] The crystal morphology was plate-like with the ***c***-axis perpendicular to the plane, similar to its structural polytype γ-Li_2IrO_3.[3] [see Fig. S1a) for the microscopic image]. Typical crystal dimensions used for Raman experiments are about 30μm $\times$ 20μm $\times$ 15μm.

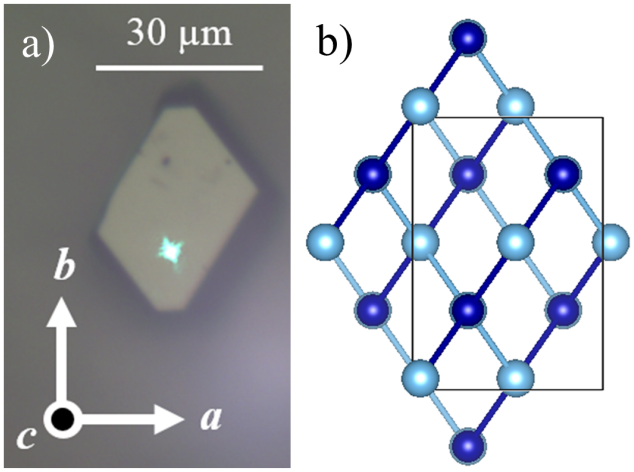

FIG. S1. (color online) a) Microscopic image of a representative β-Li_2IrO_3 crystal with a green laser at ambient pressure without the DAC, focused with a 50x microscope. b) The same orientation of the unit cell with Ir (blue and dark blue balls). Oxygen and lithium ions are not displayed for a simplicity.

S2. RAMAN MEASUREMENTS TO CHARACTERIZE BEAM-HEATING

To estimate extrinsic shifts of phonon peaks in the room temperature measurements by a local beam-heating of crystals, we carefully determined the maximised Raman signal to noise ratio that one could get while we avoided the beam-heating for all experimental setting that we used: 50x, 20x without Diamond Anvil Cell (DAC) and 20x with DAC in both green and red lasers. Figure S1a) shows a typical morphology of the crystal used in the experiment with the corresponding unit cell with the iridium network in Fig. S1b).

Figure S2 summarises the softening of selected phonon peaks with an elevating Raman laser power: we chose $A_g(1)$, $A_g(4)$, $A_g(6)$ ($A_g(4)$, $A_g(6)$) with the red laser (with the green laser) as they are stronger than other weak peaks. By fitting normalised fitted peak positions [explicitly given in Table. I from a pseudo Voigt fit, a combined function with Lorentzian and Gaussian profiles], we found that the threshold Raman power (not inducing the beam-heating effect) is about 0.7 mW without the DAC [Fig. S2a)] and about 2 mW with the DAC [Fig. S2b)]: the attenuation of light intensity by the DAC was reflected by an increased threshold laser power with the diamond cell [as compared in Figs. S2a) and S2b)]. Thus, to avoid the beam-heating, these threshold Raman laser powers were used for all relevant Raman measurements presented in this paper.

S3. RAMAN MEASUREMENTS

Raman experiments with green laser were performed with the 514 nm excitation line of an argon/krypton laser using a JobinYvon T64000 spectrometer with an energy resolution of $\sim$2.4 cm^{-1} (measured by a neon lamp). The measurements with red laser used the 632.8 nm line of a

TABLE I. Fitted peak positions with red and green Raman data upon laser power. A lens of 20x was used with the DAC and 50x lens was utilized without the DAC. The R (G) symbol in the first row means the red (green) light. The unit of frequencies is cm^{-1}.

Power	$A_g(4)G$	$A_g(6)G$	Power	$A_g(1)R$	$A_g(4)R$	$A_g(6)R$	Power (DAC)	$A_g(4)G$	Power (DAC)	$A_g(4)R$
0.40 mW	519	597	2.65 mW	182	515	617	0.52 mW	532	0.675 mW	518
0.50 mW	519	597	2.52 mW	182	516	618	0.68 mW	533	0.682 mW	519
0.60 mW	518	597	1.76 mW	182	517	620	0.92 mW	532	1.2 mW	517
0.70 mW	518	597	1.48 mW	182	517	621	1.34 mW	533	1.62 mW	518
0.80 mW	518	596	1.25 mW	183	518	623	1.7 mW	532	2 mW	518
0.91 mW	517	597	1.00 mW	183	518	622	1.98 mW	531	2.45 mW	517
1.01 mW	517	596	0.71 mW	183	520	621	2.29 mW	531	2.87 mW	516
1.17 mW	516	596	0.50 mW	184	520	623	3.16 mW	530	3.63 mW	515
1.53 mW	515	595	0.33 mW	184	520	624	3.82 mW	531	–	–
2.09 mW	513	593	0.23 mW	183	520	624	4.7 mW	530	–	–
2.50 mW	512	591	–	–	–	–	–	–	–	–

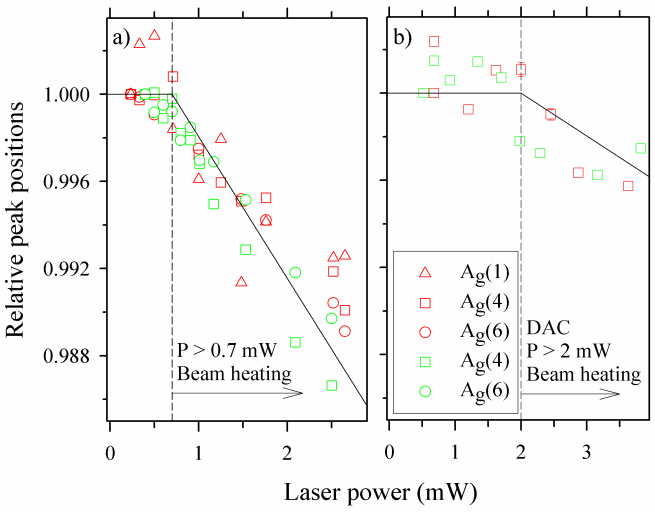

FIG. S2. (color online) Normalized positions of selected Raman peaks in terms of laser powers: a) ambient pressure without the DAC and b) with the DAC. Green (red) symbols are from the green (red) Raman light. Two vertically dashed black lines indicate estimated (based on the fits with solid black lines) strongest laser power at about 0.7 mW (2 mW) without (with) the DAC equipment, which does not induce an artificial beam-heating effect.

HeNe mixed gas laser and a Labram (Horiba Jobin-Yvon) single-grating spectrometer.[4,5]

First, we checked the Raman spectra on many crystals (more than 40 crystals) at ambient pressure with various polarizations: measurements did not show any meaningful differences in the Raman spectra, indicating homogeneous sample quality and compositions.

We also obtained Raman data with the rotated crystal with various in-plane angles along the perpendicular direction (along the $\boldsymbol{c}$-axis) of the ($\boldsymbol{ab}$)-plane-oriented crystal [see Fig. S1a)]: we confirmed that small misalignment within the plane ($\Delta\theta \lesssim 15°$) did not give very noticeable change in the spectra, ensuring reliable Raman spectra collected at even high pressure. Note that a negligible misorientation of the in-plane orientation was unavoidable such as less than 5° during measurements.

The diameter of the beam was typically $\lesssim 5$ μm at ambient pressure without the DAC, measured by a varying size of circles of gold deposited to the Al_2O_3 substrate using a sharp contrast of Raman signals from gold[6](a broad continuous intensity) and Al_2O_3[7] (a set of sharp phonon peaks). Without the DAC, we confirmed that the effective size of Raman light is approximately similar to the size of circular light observed under the microscope. Based on this, we estimated the beam size inside the DAC, to be $\lesssim 30$ μm (estimated only with the red Raman light as green Raman lights give a much smaller beam size with the DAC).

Systematic and accurate measurements were pursued by controlling various experimental conditions. For instance, the identical microscopic lens were used for all measurements: Nikon 50x/0.45 Super Long Working Distance (SLWD) and 20x/0.35 SLWD lens (the largest magnification lens available to us to be compatible with our diamond anvil cell) to use intentionally the same attenuation rate of light. It was because different types of lens would have different attenuation rates for the given light, so the beam-heating rate, which was obtained from the analysis shown in Fig. S2, would be modified accordingly.

With the green Raman light (not necessarily with the red Raman light), the continuous flow of Ar-gas has been implemented to effectively suppress Raman signals from the vibrational air scattering, mostly below about 150 cm^{-1}, which was critical to reliably identify and trace phonon peaks at the low-energy transfer especially at high-pressures. In red and green Raman experiments, different single crystals were used with a similar sample quality.

Moreover, Raman measurements on other beam positions at both ambient and finite- pressures with the DAC were tested, finding only a mere evolution of the background signal. Small linear background signals (mostly coming from the DAC) were subtracted for some high-pressure data when necessary for a better representation. A small variation of the background signal at different pressure and polarization seems to be originated from a slight redistribution of the medium liquid (see Section S2B for details) when the new pressure was applied and/or the shape and size of the Raman light was changed depending on the incident polarization of the light. All Raman measurements were made with a high-resolution (1800 grooves/mm) setting to determine phonon positions more precisely.

A. Polarized measurements with green laser (514.5 nm)

We should mention that there are some ambiguities to identify weak and overlapped Raman peaks at high-pressures. For example, a lesser number of Raman peaks has been experimentally measured reliably, compared with 18 Raman-active phonon modes obtained from the calculation [see Table. I in the main text] possibly due to their weak Raman signals. In fact, we observed very weak peak-like and shoulder features in Raman spectra at higher-pressures, but their tiny intensities for the whole pressure range explored did not allow us to do a reliable fit, so they were not marked in Fig. 2 and Table II in the main text. Moreover, in Fig. 2 in the main text, it was nearly impossible to do a reliable fit with collected Raman data at P = 4.53 and 5 GPa due to weak intensities of new Raman peaks with an increased signal from the diamond cell, thus we best estimated peak positions at P = 4.53 and 5 GPa reversely from peak positions reliably identified from P = 6.3 and 7.62 GPa, whose peaks were much better defined. Furthermore, we cannot completely rule out a possibility of mixing of sample peaks with the DAC peaks: i.e., a peak-like signal between 220 cm^{-1} and 250 cm^{-1} for a $\bar{\boldsymbol{c}}(\boldsymbol{bb})\boldsymbol{c}$ polarization in Fig. 2b) is also present even at 2.4 GPa below the transition.

Asymmetric profiles of some peaks (i.e., peaks at lower wavenumbers) could be also from the combination of multiple peaks nearby, or from the coupling with electronic response with the Ir $J_{\rm eff} = 1/2$ local moments similarly seen in Sr_2IrO_4.[4] For testing the latter case, the fitting with a Fano asymmetry profile[8] was attempted, but did not give any noticeable trend in the fitted parameters (i.e., linewidths), probably due to weak Raman intensities with relatively strong background signals with the DAC.

B. High-pressure measurements

High-pressure Raman data showed weaker signals when equipped with the DAC possibly due to the strong background signal from the DAC [see Fig. 1 in the main text], an enhanced light attenuation by the DAC and a less focusing light due to a decreased magnification of available lens (from 50x to 20x): our high-pressure setup with the DAC was not compatible with the focal length of the 50x lens, whereas Raman signals without the DAC allowed a larger magnification lens (50x). The latest factor increased a typical measurement time, more than 10 hours for a single Raman data [i.e., Fig. 2 in the main text] at one pressure and polarization to get a decent signal to noise ratio. Raman spectra was also reproduced after releasing pressure (not shown) and a similar transition pressure was found, indicating that this structural transition was reversible within the pressure explored.

Porto's notation[9] was utilised to describe the configuration of the Raman scattering experiment (in a backscattering geometry with the light propagating along the crystalline $\boldsymbol{c}$-axis). It expresses the orientation of the crystal with respect to the polarization of the laser in both the excitation and analysing directions, in a form of $k_i(E_iE_s)k_s$, where k_i (k_s) is the direction of incident (scattered) light and E_i (E_s) is the polarization of incident (scattered) light, respectively.

At high pressure, the crystallographic axes of the monoclinic structure are different from those in ambient orthorhombic structure since the $\boldsymbol{c}$-axis is no longer parallel to the the vertical axis of the laboratory frame, but tilted by 16.777°.[10] However, we did not observe any significant difference in the spectra for $\bar{\boldsymbol{c}}(\boldsymbol{ab})\boldsymbol{c}$, $\bar{\boldsymbol{c}}(\boldsymbol{ba})\boldsymbol{c}$ in Fig. 2 in the main text, indicating an insensitivity of this tilted angle of the c-axis in our measurements. This made sense, being consistent with our previous characterization measurements, which only showed some meaningful variations in the Raman spectra when the crystal was rotated by $\sim$ 15° in the ($\boldsymbol{ab}$)-plane at ambient pressure [as explained in Appendix]: this makes our analysis consistent and polarization data reliable at even high-pressures.

By symmetry analysis, Raman tensors[11] of high-pressure monoclinic structure[10] are given as

$$I_{001}(\mathrm{A_g}) = \begin{pmatrix} \mathrm{A} & \mathrm{D} & \\ \mathrm{D} & \mathrm{B} & \\ & & \mathrm{C} \end{pmatrix}$$

$$I_{001}(B_g) = \begin{pmatrix} & & \mathrm{E} \\ & & \mathrm{F} \\ \mathrm{E} & \mathrm{F} & \end{pmatrix}, \quad (1)$$

where A, B, C, D, E and F are Raman intensity components and a subscript is the direction of the propagating light.

S4. STRUCTURAL RELAXATIONS

At ambient pressure, both SOC and U were essential (as explained in the main text) to stabilize the experimental structure. Otherwise, the calculations in the absence of either U or SOC found that an initial orthorhombic structure (close to the ideal hyperhoneycomb structure) became unstable and evolved into a new type of Ir-dimerized orthorhombic crystal structure at ambient pressure, destroying the Ir $J_{\rm eff} = 1/2$ local moments [dimerized along the $\boldsymbol{c}$-axis in Fig. 4b) in the main text]. On the other hand, when we kept the converged electronic structure with the $J_{\rm eff} = 1/2$ moments and pressurized the unit cell (i.e., optimizing the cell parameters and internal coordinates with a smaller fixed volume), the orthorhombic phase without the Ir dimerization was maintained up to 10 GPa[12] as a local minima state.

S5. CALCULATIONS OF PHONON FREQUENCIES

A. DFT+U results

Here we discuss our theoretical attempts to understand origins of their mismatches in calculations and experiments. Comparing in Table I and Table II in the main text, at ambient pressure, the calculated phonon frequencies agree well with the observed phonons fitted from the Raman data except for two peaks in the spectral range between 600 and 680 cm^{-1} in the A_g channel. In particular, the frequency difference between the highest measured and calculated A_g modes is about 100 cm^{-1}, which is consistently reproduced by alternative DFT+U calculation with WIEN2K code. On the other hand, at high pressure, the calculated phonon energies agree better with the measured peaks fitted from the Raman data in Figs. 2a-d). The agreement is slightly worse at a lower energy, possibly due to less important (but non-negligible) roles of U and SOC in the dimerized structure.

We should also point out that although the overall calculating phonon frequencies match better at high pressure, a marginal mismatch of frequencies between the data and calculation is also attributed to the difference of pressures used for the comparison: a higher pressure (7.62 GPa) of the experimental data than the pressure used in the *ab-initio* calculations at (presumably) 4 GPa.[10]

B. Dynamical mean-field results on the highest A_g mode at ambient pressure

To understand the origin of the largest discrepancy between DFT+U and experimental Raman data for the high energy A_g mode, we also employed a method that can better describe strong correlation physics, in particular the non-perturbative nature of Mott insulator in the paramagnetic state. Thus, we present dynamical mean-field result on the highest A_g mode at ambient pressure.

For this calculation, we used the charge-self-consistent DFT+embedded dynamical mean-field theory (eDMFT) method,[13–15] (combined with WIEN2K[16]) including SOC to describe the *paramagnetic* Mott phase of the orthorhombic structure [see Section for computational details]. The crystal structure optimized within eDMFT (at $T = 232$ K) also showed reasonable agreement with the experimental and with the DFT-optimized structures [see Table II for details]. A finite displacement method for the highest A_g phonon mode was then used to draw the free energy versus the displacement curve for the calculation of the phonon frequency.

The paramagnetic eDMFT predicts the frequency to be 556.6 cm^{-1}. Interestingly, this result is very close to the WIEN2K magnetic DFT+U result, which is 550.9 cm^{-1}. This small (≈ 5 cm^{-1}) difference in the frequency between the paramagnetic eDMFT and magnetic DFT+U results could indicate a negligible coupling between the magnetism and the lattice. The VASP value is about 587 cm^{-1}, hence the difference between two DFT codes (different for only ~ 30 cm^{-1}) is larger than that between the DFT+U and eDMFT method. This is likely due to the basis set difference in the two DFT methods.

This is also consistent with our theoretical observation that a different magnetic order did not affect the relaxed crystal structure in the scheme of DFT+U once the Ir $J_{\rm eff} = 1/2$ state sets in.[12] However, it is also possible that the frustrated magnetism could have an important impact on determining the highest A_g phonon energy (at about 587 cm^{-1}) as this vibration is closely related to the local structure of Ir-O-Ir bond (as illustrated in Fig. 5d) in the main text), a key factor to determine exchange couplings.[12,17] Therefore, the origin of the mismatch of the highest A_g mode between the theory and experiment currently remains a topic for further investigation.

S6. COMPUTATIONAL DETAILS

A. DFT+U calculations

We employed VASP to perform the electronic structure calculations, by using the projector-augmented wave basis set.[18,19] The same parameters for plane wave energy cutoff and k-point sampling used for the previous work[12] were chosen for the total energy and structural optimizations with experimental crystal structures at ambient[1] and high pressure.[10] The calculations with and without including atomic SOC, the DFT+U on-site Coulomb interaction,[20] and magnetism in the Ir d orbital were done. All of the DFT+U calculations shown in this paper were done with the value of $U = 2$ eV, and we also checked that phonon spectra with $U = 2.5$ eV showed similar results compared to the $U = 2$ eV result (differences in

frequencies smaller than 10 cm^{-1}).

In the phonon calculation, we noticed that the lightest Li ions did not contribute high-energy modes significantly although it is the lightest ions, probably due to the much weaker ionic bonding with other ions. This makes sense because Li ions in Lithium-ion battery cathode materials are considered to be more freely removed than other constituent ions, as also experimentally observed in β-Li_2IrO_3.[21]

B. eDMFT calculations

A fully charge-self-consistent DMFT method,[14] implemented in DFT + Embedded DMFT (eDMFT) Functional code,[13] which is combined with WIEN2K code,[16] was employed for computations of electronic properties and optimizations of internal coordinates.[22] In DFT level the Perdew-Burke-Ernzerhof (PBE) generalized gradient approximation (GGA) is employed,[23] and different choices of the DFT exchange-correlation functional may affect quantitative natures of the results presented here. 2000 k-points were used to sample the first Brillouin zone with $RK_{\max} = 8.0$. A force criterion of 10^{-4} Ry/Bohr was adopted for optimizations of internal coordinates. A continuous-time quantum Monte Carlo method in the hybridization-expansion limit (CT-HYB) was used to solve the auxiliary quantum impurity problem,[24] where the Ir t_{2g} orbital was chosen as our correlated subspace in a single-site DMFT approximation. For the CT-HYB calculations, up to 10^{10} Monte Carlo steps (at $T = 58$ K) were employed for each Monte Carlo run.

In most runs, the temperature was set to be 232 K, but in some calculations with trial antiferromagnetic orders T was lowered down to 58 K. We tried to stabilize three different types of collinear antiferromagnetic orders (Néel-, zigzag-, and stripy-types), but all tried magnetic orders did not remain stable and the paramagnetic order still sets in down to $T = 58$ K, which is rather unusual for the normal DMFT calculation as the DMFT result usually overestimates the ordering temperature, which may indicate an effect of the magnetic frustration of β-Li_2IrO_3.

The reasonable hybridization window of -10 to +10 eV (with respect to the Fermi level) was chosen, and $U = 5$ eV and $J_H = 0.8$ eV of on-site Coulomb interaction parameters were used for the Ir t_{2g} orbital. This values are slightly different compared to those used in another eDMFT study of layered perovskite and pyrochlore iridates,[25,26] $(U, J) = (4.5, 0.8)$ eV, but this difference is not expected to lead to a qualitative difference.

Values of U and J_H in eDMFT are significantly larger than those adopted in DFT+U calculations because of the different choice of projectors for the correlated subspaces in both methods. For the Coulomb interactions, a simplified Ising-type (density-density terms only) approximation was applied to reduce the Monte Carlo noise, and a nominal double counting scheme was used with $n_d = 5$ for the double counting correction.

Table II and III show the optimized crystal structures for the ambient pressure orthorhombic and high-pressure monoclinic structures, starting from experimental structures, showing a reasonable agreement in both DFT+U and eDMFT results.

TABLE II. Experimental and optimized structural information of β-Li_2IrO_3 at ambient pressure. The space group is *Fddd* (No. 70, origin choice 2), where the internal coordinates for each inequivalent site are $(1/8, 1/8, z)$ for Ir and Li1/2, $(x, 1/8, 1/8)$ for O1, and (x, y, z) for O2. In the DFT+U calculation, cell parameters ($\boldsymbol{a}$, $\boldsymbol{b}$ and $\boldsymbol{c}$) were allowed to change with the fixed volume, whereas in eDMFT fixed experimental cell parameters[1] were used. Ir-Ir and Ir-O bond lengths and Ir-O-Ir bond angles in each nearest neighbor bond are also given, where the Z- (X-) bonds denote Ir-Ir bonds parallel (not parallel) to along the $\boldsymbol{c}$-axis in Fig. 4 in the main text. Zigzag-type antiferromagnetic and paramagnetic order were used for DFT+U and eDMFT ($T = 232$ K) calculations, respectively.

		Exp. (Ref. 1)	DFT+U (VASP)	DFT+U (WIEN2K)	eDMFT
	a	5.910	5.908	5.910	5.910
	b	8.456	8.440	8.456	8.456
	c (Å)	17.827	17.891	17.827	17.827
Ir (16g)	z	0.7085	0.7085	0.7096	0.7091
Li1 (16g)	z	0.0498	0.0448	0.0460	0.0459
Li2 (16g)	z	0.8695	0.8775	0.8783	0.8775
O1 (16e)	x	0.8572	0.8588	0.8614	0.8638
O2 (32h)	x	0.6311	0.6320	0.6294	0.6277
	y	0.3642	0.3654	0.3669	0.3666
	z	0.0383	0.0384	0.0389	0.0393
$d_{\mathrm{Ir-Ir}}$	Z	2.979	2.988	3.0203	3.000
(in Å)	X	2.973	2.973	2.9536	2.960
$d_{\mathrm{Ir-O}}$	Z	2.025	2.035	2.0573	2.059
(averaged)	X	2.025	2.029	2.0356	2.043
$\theta_{\mathrm{Ir-O-Ir}}$	Z	94.68	94.50	94.45	93.50
(degree)	X	94.43	94.23	93.02	92.86

* Present address: Rutgers Center for Emergent Materials and Department of Physics and Astronomy, Rutgers University, Piscataway, New Jersey 08854, USA

[1] T. Takayama, A. Kato, R. Dinnebier, J. Nuss, H. Kono, L. S. I. Veiga, G. Fabbris, D. Haskel, and H. Takagi, Phys. Rev. Lett. **114**, 077202 (2015).

[2] A. Glamazda, P. Lemmens, S.-H. Do, Y. S. Choi, and K.-Y. Choi, Nat. Commun. **7**, 12286 (2016).

TABLE III. Experimental and optimized lattice parameters and internal coordinates of β-Li_2IrO_3 with $C2/c$ (No. 15) space group symmetry at high pressure. In this calculation, lattice parameters of $\boldsymbol{a}$, $\boldsymbol{b}$, $\boldsymbol{c}$ and β were optimized in the DFT and DFT+U calculations with a fixed volume. Values of pressure measured in the experiment and DFT-estimation are shown in the top row. Ir-Ir and Ir-O bond lengths and Ir-O-Ir bond angles in each nearest neighbor bond are shown below.

		Exp. (Ref. 10)	DFT+U (with SOC)	DFT (no SOC)
	P (GPa)	4.4	5.0	5.4
	a	5.7930	5.7752	5.7485
	b	8.0824	8.0408	8.0319
	c (Å)	9.144	9.1951	9.2365
	β (degree)	106.777	106.263	106.016
Ir	x	0.4219	0.4235	0.4238
	y	0.3844	0.3877	0.3887
	z	0.0780	0.0772	0.0770
Li1	x	0.244	0.2434	0.2448
	y	0.632	0.6382	0.6401
	z	0.246	0.2436	0.2442
Li2	x	0.926	0.9270	0.9261
	y	0.625	0.6177	0.6165
	z	0.589	0.5936	0.5932
O1	x	0.7341	0.7320	0.7310
	y	0.3859	0.3895	0.3916
	z	0.2535	0.2542	0.2544
O2	x	0.9024	0.9024	0.9015
	y	0.3598	0.3596	0.3585
	z	0.5792	0.5811	0.5812
O3	x	0.4140	0.4118	0.4142
	y	0.3719	0.3625	0.3607
	z	0.5859	0.5870	0.5886
$d_{\mathrm{Ir-Ir}}$ (in Å)	dimer	2.6609	2.5999	2.5838
	non-dimer	3.0136	3.0513	3.0697
$d_{\mathrm{Ir-O}}$ (averaged)	dimer	2.012	2.0098	2.0137
	non-dimer	1.970	2.0235	2.0232
$\theta_{\mathrm{Ir-O-Ir}}$ (avg. deg.)	dimer	84.3	80.6	79.8
	non-dimer	97.4	97.9	98.7

[3] K. A. Modic, T. E. Smidt, I. Kimchi, N. P. Breznay, A. Biffin, S. Choi, R. D. Johnson, R. Coldea, P. Watkins-Curry, G. T. McCandless, J. Y. Chan, F. Gandara, Z. Islam, A. Vishwanath, A. Shekhter, R. D. McDonald, and J. G. Analytis, Nat. Commun. **5**, 4203 (2014).

[4] H. Gretarsson, N. H. Sung, M. Höppner, B. J. Kim, B. Keimer, and M. Le Tacon, Phys. Rev. Lett. **116**, 136401 (2016).

[5] S.-M. Souliou, J. Chaloupka, G. Khaliullin, G. Ryu, A. Jain, B. J. Kim, M. Le Tacon, and B. Keimer, Phys. Rev. Lett. **119**, 067201 (2017).

[6] http://rruff.info/Gold/

[7] P. G. Li, M. Lei, W. H. Tang, Mater. Lett. **64**, 161 (2010).

[8] U. Fano, Phys. Rev. **124**, 1866 (1961).

[9] T. C. Damen, S. P. S. Porto, and B. Tell, Phys. Rev. **142**, 570 (1966).

[10] L. S. I. Veiga, M. Etter, K. Glazyrin, F. Sun, C. A. Escanhoela, Jr. G. Fabbris, J. R. L. Mardegan, P. S. Malavi, Y. Deng, P. P. Stavropoulos, H.-Y. Kee, W. G. Yang, M. van Veenendaal, J. S. Schilling, T. Takayama, H. Takagi, and D. Haskel, Phys. Rev. B **96**, 140402(R) (2017).

[11] Bilbao Crystallographic Server, http://www.cryst.ehu.es/

[12] H.-S. Kim, Y. B. Kim, and H.-Y. Kee, Phys. Rev. B **94**, 245127 (2016).

[13] http://hauleweb.rutgers.edu/tutorials/

[14] K. Haule, C.-H. Yee, and K. Kim, Phys. Rev. B **81**, 195107 (2010).

[15] K. Haule, J. Phys. Soc. Jpn. **87**, 041005 (2018).

[16] P. Blaha, K. Schwarz, G. K. H. Madsen, D. Kvasnicka, and J. Luitz, *WIEN2k, An Augmented Plane Wave + Local Orbitals Program for Calculating Crystal Properties* (Karlheinz Schwarz, Techn. Universität Wien, Austria, 2001).

[17] S. M. Winter, Y. Li, H. O. Jeschke, and R. Valentí, Phys. Rev. B **93**, 214431 (2016).

[18] G. Kresse, and J. Furthmüller, Phys. Rev. B **54**, 11169 (1996).

[19] G. Kresse, and D. Joubert, Phys. Rev. B **59**, 1758 (1999).

[20] S. L. Dudarev, G. A. Botton, S. Y. Savrasov, C. J. Humphreys, and A. P. Sutton, Phys. Rev. B **57**, 1505 (1998).

[21] P. E. Pearce, A. J. Perez, G. Rousse, M. Saubanère, D. Batuk, D. Foix, E. McCalla, A. M. Abakumov, G. Van Tendeloo, M.-L. Doublet, and J.-M. Tarascon, Nat. Mater. **16**, 580 (2017).

[22] K. Haule and G. L. Pascut, Phys. Rev. B **94**, 195146 (2016).

[23] J. P. Perdew, K. Burke, and M. Ernzerhof, Phys. Rev. Lett. **77**, 3865 (1996).

[24] K. Haule, Phys. Rev. B **75**, 155113 (2007).

[25] H. Zhang, K. Haule, and D. Vanderbilt, Phys. Rev. Lett. **111**, 246402 (2013).

[26] H. Zhang, K. Haule, and D. Vanderbilt, Phys. Rev. Lett. **118**, 026404 (2017).